

Article

New Ferrocene-Based Metalloligand with Two Triazole Carboxamide Pendant Arms and Its Iron(II) Complex: Synthesis, Crystal Structure, ^{57}Fe Mössbauer Spectroscopy, Magnetic Properties and Theoretical Calculations

Peter Antal ¹, Ivan Nemeč ^{1,2}, Jiří Pechoušek ³ and Radovan Herchel ^{1,*}

¹ Department of Inorganic Chemistry, Faculty of Science, Palacký University Olomouc, 17. Listopadu 12, 77146 Olomouc, Czech Republic

² Central European Institute of Technology, CEITEC BUT, Technická 3058/10, 61600 Brno, Czech Republic

³ Department of Experimental Physics, Faculty of Science, Palacký University Olomouc, 17. Listopadu 12, 77146 Olomouc, Czech Republic

* Correspondence: radovan.herchel@upol.cz

Abstract: The new ferrocene-based metalloligand bis (*N*-4-[3,5-di-(2-pyridyl)-1,2,4-triazoyl])ferrocene carboxamide (**L**) was prepared through derivatization of 1,1'-ferrocenedicarboxylic acid with 4-amino-3,5-di(pyridyl)-4*H*-1,2,4-triazole. The composition and purity of **L** in the solid state was determined with elemental analysis, FT-IR spectroscopy, and its crystal structure with single-crystal X-ray analysis, which revealed that the substituted cyclopentadienyl rings adopt the antiperiplanar conformation and the crystal structure of **L** is stabilized by O–H...N and N–H...O hydrogen bonds. The molecular properties of **L** in solution were investigated with NMR and UV-VIS spectroscopies, and cyclic voltammetry disclosed irreversible redox behavior providing one oxidation peak at $E_{1/2} = 1.133$ V vs. SHE. Furthermore, the polymeric Fe^{II} complex $\{\text{Fe}(\text{L})(\text{C}(\text{CN})_3)_2\}_n$ (**1**) was prepared and characterized with elemental analysis, FT-IR spectroscopy, ^{57}Fe Mössbauer spectroscopy, and magnetic measurements. The last two methods confirmed that a mixture of low- and high-spin species is present in **1**; however, the spin crossover properties were absent. The presented study was also supported by theoretical calculations at the DFT/TD-DFT level of theory using TPSS and TPSSh functionals.

Keywords: metalloligand; abpt; ferrocene; iron(II) complex; Mössbauer spectroscopy; magnetic properties; DFT calculations



Citation: Antal, P.; Nemeč, I.; Pechoušek, J.; Herchel, R. New Ferrocene-Based Metalloligand with Two Triazole Carboxamide Pendant Arms and Its Iron(II) Complex: Synthesis, Crystal Structure, ^{57}Fe Mössbauer Spectroscopy, Magnetic Properties and Theoretical Calculations. *Inorganics* **2022**, *10*, 199. <https://doi.org/10.3390/inorganics10110199>

Academic Editor: Lubov Snegur

Received: 30 September 2022

Accepted: 3 November 2022

Published: 7 November 2022

Publisher's Note: MDPI stays neutral with regard to jurisdictional claims in published maps and institutional affiliations.



Copyright: © 2022 by the authors. Licensee MDPI, Basel, Switzerland. This article is an open access article distributed under the terms and conditions of the Creative Commons Attribution (CC BY) license (<https://creativecommons.org/licenses/by/4.0/>).

1. Introduction

Multifunctional materials represent a group of any materials that integrally combine two or more applicable properties. There is currently great interest in the study and design of multifunctional molecular materials that have spin-switching as one of the functions, not only for fundamental reasons but also in attempts to make innovative multifunctional devices. However, it is relatively hard to design a single molecular material capable of performing multiple functions. One of the synthetic ways involves sophisticated design of the ligands used. Traditional ligand functions include binding to a metal center and provision of steric hindrance or binding groups. In this context, the use of a metalloligand is a powerful synthetic strategy with considerable advantages. The metalloligand is a suitably designed complex which may act as a ligand capable of placing appended functional groups in limited directions, and, therefore, such functional groups can bind to secondary metal ions in a limited geometrical manner. The metalloligand approach presents a facile way to obtain multinuclear complexes with a specific combination of a primary metal ion (within the metalloligand) and a secondary metal ion (within the resultant complex).

Another advantage is that the structural rigidity of the metalloligand often causes the structural motif of the resultant complex to be highly predictable [1–4].

In this context, ferrocene derivatives bearing donor substituents are suitable for the metalloligand approach and thus are very useful for the development of specifically designed multinuclear metal complexes [5,6]. One of the well-known examples of a ferrocene-based metalloligand is 1,1'-bis-(phenylphosphino)ferrocene, which is often used as a ligand in catalysis and for the generation of novel coordination compounds with a wide range of coordination geometries and properties [7].

Spin crossover (SCO) complexes show dynamic switching between high-spin and low-spin states upon external stimuli, such as temperature and/or pressure changes, as well as light radiation treatment. This transition leads to drastic changes in electronic, magnetic, optical, and mechanical properties giving them a bistable character, which could be useful for the design of molecular devices for data storage or optical displays [8–11]. Multifunctional ligands in the field of SCO are very topical due to the fact that they provide the resulting SCO complex with their secondary function, resulting in further associated properties such as porosity, electrical conductivity, magnetic order, liquid crystal, and non-linear optical activity [8–11]. Coupling the ferrocenyl group, a part with well-defined redox properties, to ligands capable of inducing SCO affords the possibility to investigate synergies between SCO and the other properties and ultimately to find new physical phenomena and potential new applications.

In this context, ferrocenyl-containing pyridyl-triazole ligands were previously studied as suitable building blocks for the synthesis of SCO complexes with redox/electron-transfer as the second function [12]. Generally, triazole-based ligands are widely studied and used to build switchable coordination compounds. For example, complexes of iron(II) comprising the abpt ligand (4-amino-3,5-di(pyridyl)-4*H*-1,2,4-triazole) with the general formula $[\text{Fe}(\text{abpt})_2\text{A}_2]$, where A stands for various pseudohalides (NCS^- , NCSe^- , $\text{N}(\text{CN})_2^-$, $\text{C}(\text{CN})_3^-$, etc.) or polycyanometallates ($[\text{Fe}(\text{CN})_5(\text{NO})]^{2-}$, $[\text{Pt}(\text{CN})_6]^{2-}$, $[\text{Ni}(\text{CN})_4]^{2-}$, etc.), were widely studied, and all exhibit spin crossover behavior (SCO) [13,14]. Ferrocenyl and analogous cobaltocenyl-containing abpt ligands (Figure 1) were synthesized, and complexation with Co^{II} , Cu^{II} , Zn^{II} , and Cd^{II} was studied [15,16].

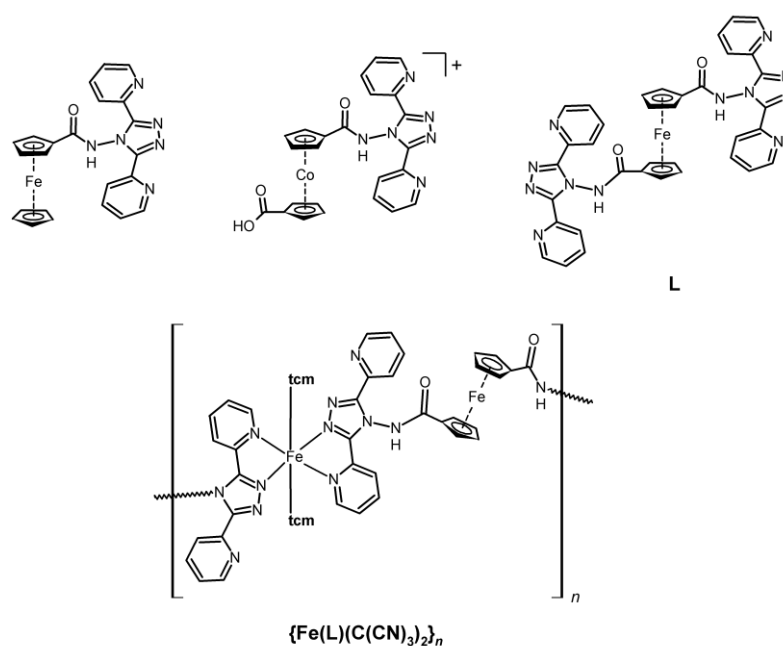


Figure 1. The structural formulae of ligands discussed in the text and the metalloligand L studied herein (top). The proposed structural formula of polymeric Fe^{II} complex 1 (tcm = tricyanomethanide anion) (bottom).

Here, we report the synthesis and characterization of the new ferrocene-based metalloligand **L** with two triazole carboxamide pendant arms and its polymeric Fe^{II} complex $(\{\text{Fe}(\text{L})(\text{C}(\text{CN})_3)_2\}_n (\mathbf{1}))$.

2. Results and Discussion

2.1. Synthesis of Metalloligand **L** and Fe^{II} Complex

The ligand **L** was prepared with a two-step synthesis. In the first step 1,1'-ferrocenedicarboxylic acid was converted to the corresponding dichloride, which was used in the following reaction with abpt to give the product. After purification through column chromatography, the ligand was isolated as an orange solid. The identity and purity of **L** was confirmed on the basis of elemental analysis and multinuclear (^1H , ^{13}C) NMR data. Single crystals suitable for X-ray structure analysis were prepared with slow evaporation of a chloroform-methanol solution.

The Fe^{II} complex (**1**) was prepared through the reaction of equimolar amounts of **L**, $\text{FeCl}_2 \cdot 4\text{H}_2\text{O}$, and potassium tricyanomethanide in a mixture of methanol-DCM under an argon atmosphere. The identity of the complex was confirmed on the basis of elemental analysis, FTIR, and ^{57}Fe Mössbauer data. Unfortunately, as a result of the low solubility, all experiments to prepare crystals suitable for X-ray structure analysis through recrystallization from different solvent systems or using different temperature gradients, slow diffusion, or hydrothermal synthesis were unsuccessful. Bidentate ferrocene-based ligands containing flexible spacer, including amide group, are inclined to form oligomers or low-dimensional polymers [17–21]. Based on this fact and the results of analyses, we suppose a polymeric structure of the Fe^{II} complex **1**.

2.2. Description of the Crystal Structure of the Ligand (**L**)

The ligand **L** crystallizes in the monoclinic space group $P2_1/c$ with four molecules of the ligand in the asymmetric unit ($Z = 4$). The molecular structure of **L** is shown in Figure 2 (additional structural data are available in the Supporting Information, Table S1).

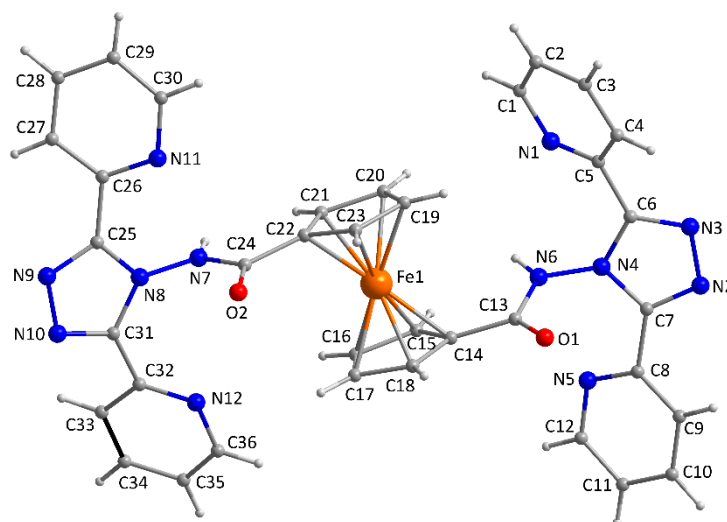


Figure 2. The molecular structure of the studied metalloligand **L** with atom-numbering of non-hydrogen atoms.

The average values of the Fe–C and C–C bond lengths in the ferrocenyl unit of **L** are 2.04 and 1.41 Å, respectively (Table 1). The average C–C–C bond angles in the cyclopentadienyl (Cp) rings are 108.0°. These values agree with those of ferrocene reported elsewhere within the experimental error [22–24]. The Cp rings in the crystal structure of the ligand **L** are slightly tilted by an angle of 2.7°. The conformation of the disubstituted ferrocenyl ligands can be defined by the torsion angle τ , defined as the torsion angle of

$C_A-Cp_A-Cp_B-C_B$, where C_A and C_B are carbon atoms bonded to the substituents and Cp_A and Cp_B are the centroids of the Cp rings [5]. The Cp rings in the crystal structure of **L** adopt the antiperiplanar conformation ($\tau = 157.8^\circ$). The dihedral angles between the mean planes of the rings of cyclopentadienyl and triazole equal 88.0° (for cyclopentadienyl and triazole defined by the atoms C14-C18, and N2-3, N5, C6-7, respectively), and 79.4° (for C19-23 and N8-10, C30-31). The pyridine and triazole rings of the abpt arms of **L** deviate significantly from planarity. The dihedral angles between the mean planes of the triazole and pyridine rings are equal to 40.4 and 26.9° for the first and 49.3 and 38.3° for the second arm.

Table 1. Selected bond lengths (Å) and angles ($^\circ$) in **L**.

Fe1-C14	2.026(7)	Fe1-C19	2.029(7)
Fe1-C15	2.025(6)	Fe1-C20	2.038(7)
Fe1-C16	2.051(7)	Fe1-C21	2.046(7)
Fe1-C17	2.034(7)	Fe1-C22	2.023(7)
Fe1-C18	2.042(8)	Fe1-C23	2.019(6)
C19-C20-C21	109.1(7)	C14-C15-C16	108.4(7)
C20-C21-C22	108.3(7)	C15-C16-C17	106.8(7)
C21-C22-C23	107.0(7)	C16-C17-C18	110.4(7)
C22-C23-C19	108.8(6)	C17-C18-C14	106.4(7)
C23-C19-C20	106.3(7)	C18-C14-C15	107.9(8)

The crystal structure of **L** is stabilized by O–H...N and N–H...O hydrogen bonds (Figure 3a). The N–H...O hydrogen bonds, between the carboxamide groups of neighboring molecules (N6–H6...O6), self-assemble the molecules into chains parallel to the *a* axis. The chains are interconnected through molecules of water (O7) by hydrogen bonds (O7–H7A...N2 and N7–H7...O7), which link neighboring chains into a two-dimensional network parallel with the plane *ac* (Figure S5a). An additional C–H... π interaction connects the layers into a three-dimensional network (Figure 3b, ESI Figure S5b).

2.3. UV-VIS Absorption Spectroscopic Studies

The absorption spectrum of **L** obtained in dichloromethane (Figure S6; $c = 2.1$ mmol/L) shows bands at 346 nm ($444 \text{ L}\cdot\text{mol}^{-1}\cdot\text{cm}^{-1}$) and 448 nm ($241 \text{ L}\cdot\text{mol}^{-1}\cdot\text{cm}^{-1}$), which correspond to the π - π^* transitions from the ferrocenyl to the pyridyl-triazole moiety and to d-d transitions, probably mixed with d- π^* transitions, respectively. Due to high intensity, further absorption bands in the UV region were studied at a lower concentration (Figure S6; $c = 43.2 \mu\text{mol/L}$). These bands at 228, 256, and 292 nm with molar absorption coefficients $26,530$, $31,729$, and $35,417 \text{ L}\cdot\text{mol}^{-1}\cdot\text{cm}^{-1}$, respectively, correspond to the π - π^* transitions from the ferrocenyl to the pyridyl-triazole moiety [25,26].

2.4. Electrochemical Properties

The electrochemical properties of **L** were studied with cyclic voltammetry in CH_3CN ($1 \times 10^{-3} \text{ M}$) containing tetrabutylammonium perchlorate as the supporting electrolyte. The cyclic voltammogram of **L** shows irreversible redox behavior providing one oxidation peak at $E_{1/2} = 1.133 \text{ V vs. SHE}$ ($\Delta E_p = 90 \text{ mV}$; Figure 4). The large anodic to cathodic peak current ratio ($i_a/i_c = 3.62$) is attributed to substrate deposition at the working electrode [27]. The observed value of $E_{1/2}$ is shifted to more positive potentials in comparison with ferrocene ($E_{1/2} = 0.619 \text{ V vs. SHE}$), owing to the substitution of the cyclopentadienyl rings with electron withdrawing carboxamide groups. A similar phenomenon was observed for several ferrocene derivatives containing a carboxamide group [28].

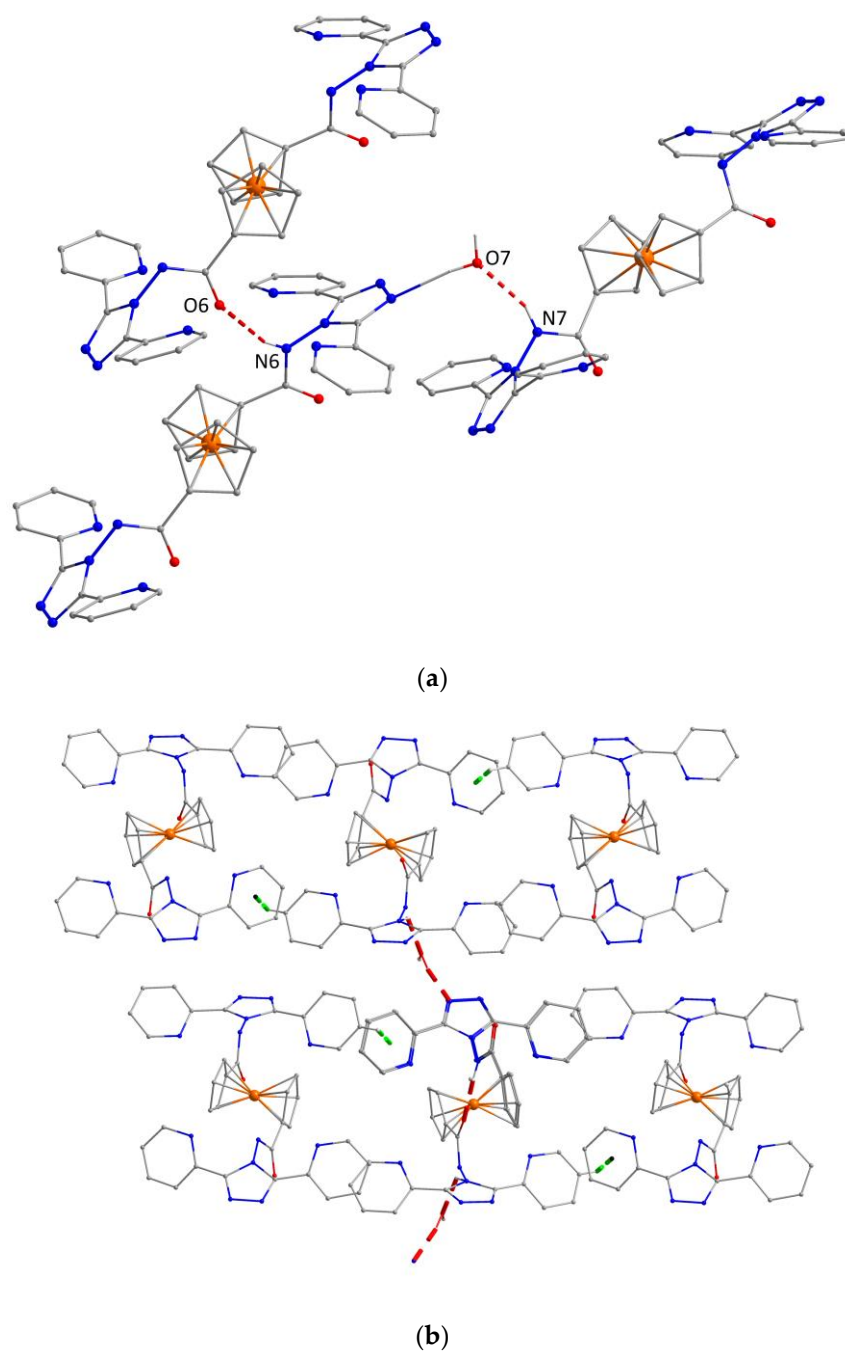


Figure 3. (a) A part of the crystal structure of **L** showing O–H···N and N–H···O hydrogen bonds (red dashed lines). Hydrogen atoms not involved in hydrogen bonding have been omitted for the sake of clarity. (b) Capped stick representation of **L**, showing a three-dimensional network formed by hydrogen bonds (red dashed lines) and C–H··· π interaction (green dashed lines).

2.5. Magnetic Properties

The magnetic properties of **1** were measured in the temperature range of 2 to 300 K and are displayed as the effective magnetic moment (μ_{eff}) in Figure 5. The μ_{eff} is practically constant in the whole temperature range adopting the value of $2.1 \mu_{\text{B}}$.

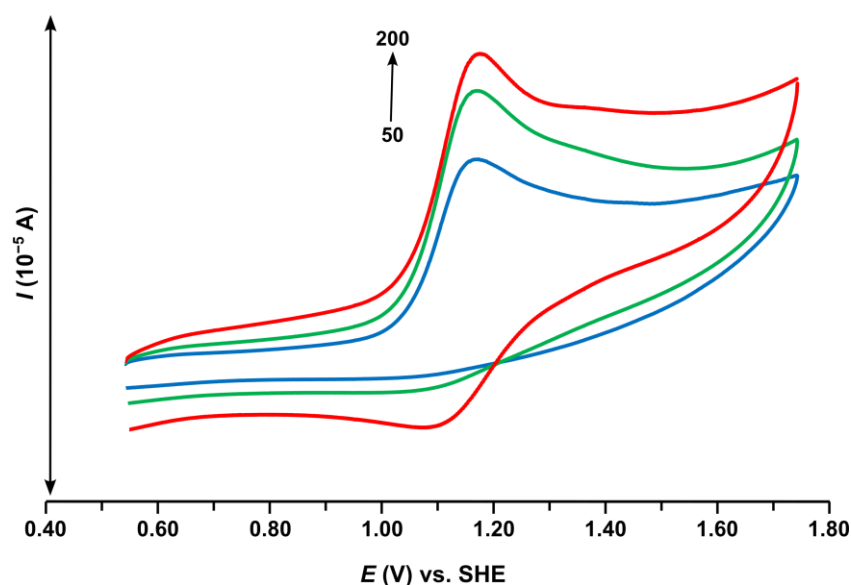


Figure 4. Cyclic voltammograms of **L** ($c \approx 1$ mM) recorded under an argon atmosphere in 0.1 M TBAP acetonitrile solution with a glassy carbon working electrode at the scan rates of 200 (red), 100 (green), and 50 mV/s (blue).

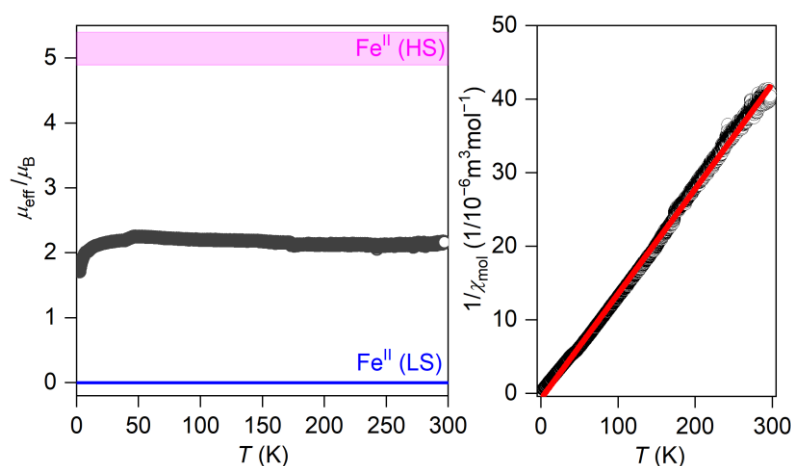


Figure 5. The temperature dependence of the effective magnetic moment (calculated from the magnetization measured at $B = 0.2$ T) of **1** (left). Blue and magenta lines show typical values for LS and HS Fe^{II} species. The linear regression to the reciprocal molar susceptibility according to Equation (1) (right).

The theoretical value of Fe^{II} in the high-spin (HS) state should span the interval between $4.90 \mu_{\text{B}}$ ($g = 2.00$) and $5.39 \mu_{\text{eff}}$ ($g = 2.20$), while the low-spin (LS) state of Fe^{II} is diamagnetic (μ_{B} is Bohr magneton). Thus, the experimental magnetic data clearly say that Fe^{II} coordinated to **L** and tcm anions in **1** is present both in the LS and HS spin states and evidently spin crossover is not induced by a temperature change. The average value of μ_{eff} of **1** was used to estimate the ratio of LS and HS according to Equation (1) based on the Curie–Weiss law:

$$\chi_{\text{mol}} = x_{\text{HS}}\chi_{\text{HS}} + (1 - x_{\text{HS}})\chi_{\text{LS}} = x_{\text{HS}} \frac{N_{\text{A}}\mu_0\mu_{\text{B}}^2}{3k} S_{\text{HS}}(S_{\text{HS}} + 1) \frac{g_{\text{HS}}^2}{T - \Theta} \quad (1)$$

where N_{A} is the Avogadro constant, μ_0 is the permeability of vacuum, k is the Boltzmann constant, x_{HS} is the molar ratio of the HS species, and χ_{HS} and χ_{LS} are the molar susceptibilities of the HS and LS states, respectively. Linear regression of $1/\chi_{\text{mol}}$ provided the

value of the Weiss constant $\Theta = -5.0$ K and the product value of $x_{\text{HS}} \cdot g_{\text{HS}}^2 = 0.743$ (Figure 5). Therefore, x_{HS} should cover the interval between 19% and 15% as calculated with $g = 2.00$ and $g = 2.20$, respectively.

2.6. ^{57}Fe Mössbauer Spectroscopy

The Mössbauer spectroscopy of ^{57}Fe was applied to compound **1**. First, the low temperature spectrum of **1** was acquired at 5 K, and it consists of three doublets (Figure 6a). The first doublet was fitted with the isomer shift $\delta = 0.53$ $\text{mm}\cdot\text{s}^{-1}$ and the quadrupole splitting $\Delta E_{\text{Q}} = 2.28$ $\text{mm}\cdot\text{s}^{-1}$. These isomer shift and quadrupole splitting values are similar with the values for ferrocene and its amide derivatives [29,30]; therefore, this signal was assigned to iron ions coordinated to cyclopentadienyl moieties labelled as $\{\text{Fe}(\text{Cp})\}$ in Table 2. The second doublet was fitted with the isomer shift $\delta = 0.41$ $\text{mm}\cdot\text{s}^{-1}$ and the quadrupole splitting, $\Delta E_{\text{Q}} = 0.48$ $\text{mm}\cdot\text{s}^{-1}$. The isomer shift value and the quadrupole splitting are similar with the values for octahedral low-spin Fe^{II} complexes [31] and was assigned to iron ions coordinated to abpt moieties labelled as $\{\text{Fe}(\text{abpt})\}^{\text{LS}}$ in Table 2. The third doublet was fitted with the isomer shift $\delta = 1.18$ $\text{mm}\cdot\text{s}^{-1}$ and the quadrupole splitting $\Delta E_{\text{Q}} = 3.15$ $\text{mm}\cdot\text{s}^{-1}$. Such values of the parameters are similar with the values for octahedral high-spin Fe^{II} complexes, and thus can be assigned to $\{\text{Fe}(\text{abpt})\}^{\text{HS}}$. The integrated areas of the doublets were found to be in the ratio 37:13:50 for $\{\text{Fe}(\text{abpt})\}^{\text{LS}}:\{\text{Fe}(\text{abpt})\}^{\text{HS}}:\{\text{Fe}(\text{Cp})\}$. This ratio corresponds to the analysis of magnetic data. Next, the room temperature (298 K) spectrum was measured, and again it consists of three doublets (Figure 6b). Analogous analysis resulted in parameters listed in Table 2. There is a small decrease of the isomer shift and the quadrupole splitting values upon increasing the temperature, which is due to the second-order Doppler effect and due to the temperature-dependent Boltzmann population of the iron(II) d-orbitals split by low-symmetry ligand field, respectively [32]. The integrated areas of the reported doublets were found to be in the ratio 50:13:37 for $\{\text{Fe}(\text{abpt})\}^{\text{LS}}:\{\text{Fe}(\text{abpt})\}^{\text{HS}}:\{\text{Fe}(\text{Cp})\}$. Evidently, the ratio of the three signals changed with the temperature, which would usually indicate spin crossover. However, as the magnetic measurements excluded this phenomenon, the change in the intensities can be assigned to different temperature dependence of Lamb–Mössbauer factors of these species. Moreover, the analyzed parameters of δ and ΔE_{Q} are consistent with the parameters found in other Fe^{II} complexes [33,34] with the abpt ligand as showed in Table 2, thus confirming the correct assignment in the case of compound **1**.

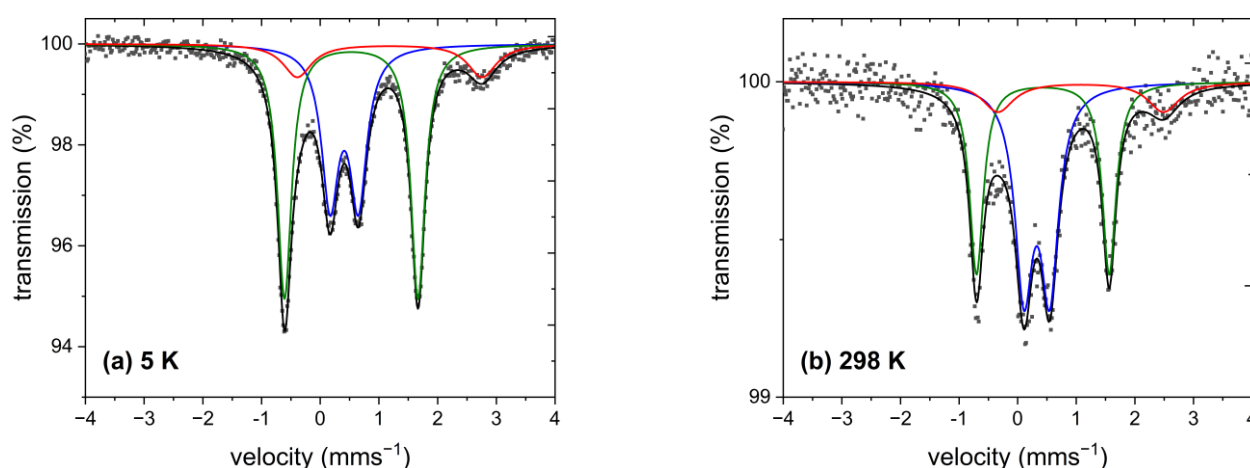


Figure 6. ^{57}Fe Mössbauer spectra for **1** at $T = 5$ (a) and at $T = 298$ K (b). The dots represent the experimental data, and the calculated data are shown with a full black line. The respective subspectra are colored as $\{\text{Fe}(\text{abpt})\}^{\text{LS}}$ in blue, $\{\text{Fe}(\text{abpt})\}^{\text{HS}}$ in red, and $\{\text{Fe}(\text{Cp})\}$ in green color.

Table 2. Experimentally determined ^{57}Fe Mössbauer parameters for **1** and other Fe^{II} complexes with abpt ligand ^a.

Experimental data ^b	$\{\text{Fe}(\text{abpt})\}^{\text{LS}}$		$\{\text{Fe}(\text{abpt})\}^{\text{HS}}$		$\{\text{Fe}(\text{Cp})\}$	
	δ	ΔE_{Q}	δ	ΔE_{Q}	δ	ΔE_{Q}
1 (5 K)	0.41(1)	0.48(1)	1.18(1)	3.15(2)	0.53(1)	2.28(1)
1 (298 K)	0.33(1)	0.44(1)	1.08(4)	2.83(1)	0.43(1)	2.27(1)
$[\text{Fe}(\text{DAPP})(\text{abpt})](\text{ClO}_4)_2$ (80 K) [33]	0.570(1)	0.419(1)				
$[\text{Fe}(\text{DAPP})(\text{abpt})](\text{ClO}_4)_2$ (211 K) [33]			1.022(1)	1.385(2)		
$[\text{Fe}(\text{abpt})_2(\mu\text{-Fe}(\text{CN})_5(\text{NO}))_n]$ (25 K) [34]	0.517	0.478	1.065	3.736		
DFT calculated data	δ	ΔE_{Q}	δ	ΔE_{Q}	δ	ΔE_{Q}
1' (LS)	0.54	0.63			0.60	2.24
					0.60	2.25
1' (HS)			1.14	3.28	0.60	2.24
					0.60	2.25
$[\text{Fe}(\text{DAPP})(\text{abpt})]^{2+}$ (LS)	0.61	0.25				
$[\text{Fe}(\text{DAPP})(\text{abpt})]^{2+}$ (HS)			1.06	3.41		

^a LS and HS labels correspond to low-spin and high-spin Fe^{II} ions coordinated by abpt moieties $\{\text{Fe}(\text{abpt})\}$, and $\{\text{Fe}(\text{Cp})\}$ and correspond to low-spin Fe^{II} in the ferrocene-subunit of metalloligand **L**; DAPP = bis(3-aminopropyl)(2-pyridylmethyl)amine. ^b values of the isomer shifts and quadrupole splitting are in $\text{mm}\cdot\text{s}^{-1}$.

2.7. Theoretical Calculations

First, the molecular and electronic structure of the metalloligand **L** was theoretically studied at the DFT/TD-DFT level of theory using ORCA 5.0 software. The molecular structure of the metalloligand **L** was optimized with TPSS functional upon application of the SMD solvation model for dichloromethane (Figure 7, Table S2). Next, the optimized geometry underwent TD-DFT calculations with TPSSh functional comprising three hundred excited states. The resulting absorption spectrum is shown in Figure 8. In order to analyze the calculated spectrum, Multiwfn software was utilized [35]. Herein, the intensities calculated from the TD-DFT oscillator strengths were transformed into the molar absorption coefficients as implemented in Multiwfn. The compound **L** was divided into five fragments as graphically depicted in Figure 7. The iron atom is labelled as M, two carboxamide-functionalized cyclopentadienes are labelled as L2 and L3, and dipyriddy-triazole units are labelled as L4 and L5. This enabled us to calculate interfragment charge transfer during electron excitation (IFCT) [36] and analyze the individual contribution of the metal-centered states (MC), intra-ligand states (IL), metal-to-ligand charge transfer states (MLCT), ligand to-metal charge transfer states (LMCT), and ligand-to-ligand charge transfer states (LLCT) as showed in Figure 8. Evidently, the strongest absorption band located at $\sim 33,000\text{ cm}^{-1}$ is based on the dominant contributions of the intra-ligand excitation of the L4 and L5 fragments with a minor contribution of MLCT (Figure 8a). Much weaker absorption in the visible part of the spectrum ($\sim 21,800\text{ cm}^{-1}$) is mainly caused by the combinations of the MC and MLCT contributions (Figure 8b), where L2 and L3 fragments based on cyclopentadiene and also L4 and L5 fragments based on abpt are involved within the MLCT contributions. To conclude, the main features of the UV/VIS spectrum of **L** reproduced with TD-DFT and IFCT analyses helped us to understand the origin of these electron excitations.

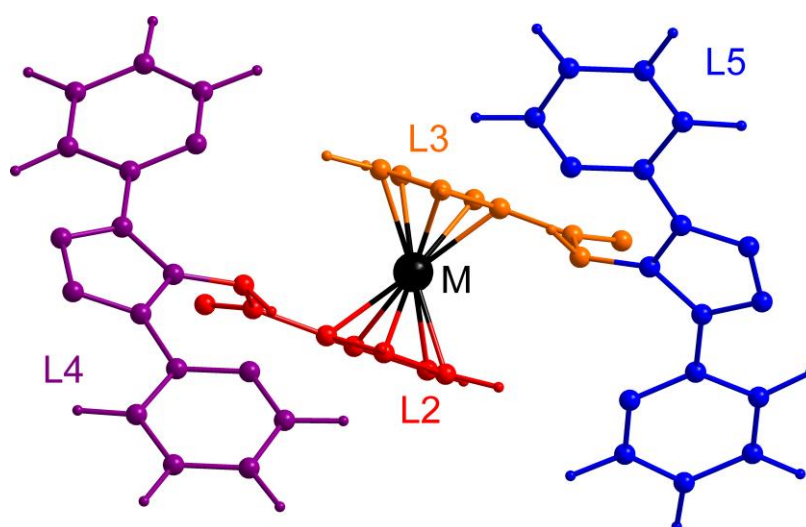


Figure 7. The DFT optimized molecular structure of L used for TD-DFT calculations with graphically marked fragments.

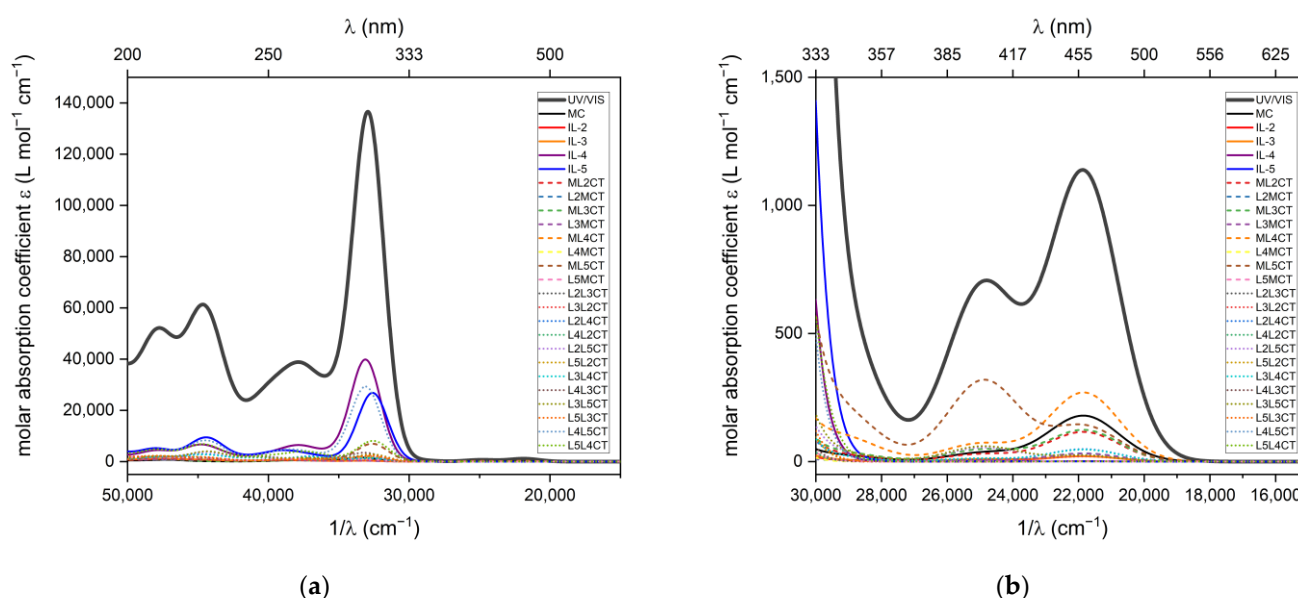


Figure 8. The TD-DFT calculated absorption spectrum of L in the UV (a) and visible part (b) with the individual fragment contributions as deduced from IFCT analysis. The metal-centered states (MC), intra-ligand states (IL), metal-to-ligand charge transfer states (MLCT), ligand to-metal charge transfer states (LMCT), and ligand-to-ligand charge transfer states (LLCT) are numbered according to the molecular fragments showed in Figure 7. The spectrum was calculated by setting value of 2500 cm^{-1} for full width at half maximum (FWHM).

Next, we also analyzed the properties of **1**, and with the aim to support the observation from ^{57}Fe Mössbauer spectroscopy, a part of the presumed polymeric structure of **1** labelled as **1'** was optimized both for the LS and HS states using TPSS functional together with SMD solvation model for water (Figure 9, Tables S3 and S4). Such functional was utilized for the geometry optimization in the computation study by Krewald et al. focused on the ^{57}Fe Mössbauer spectroscopy [37].

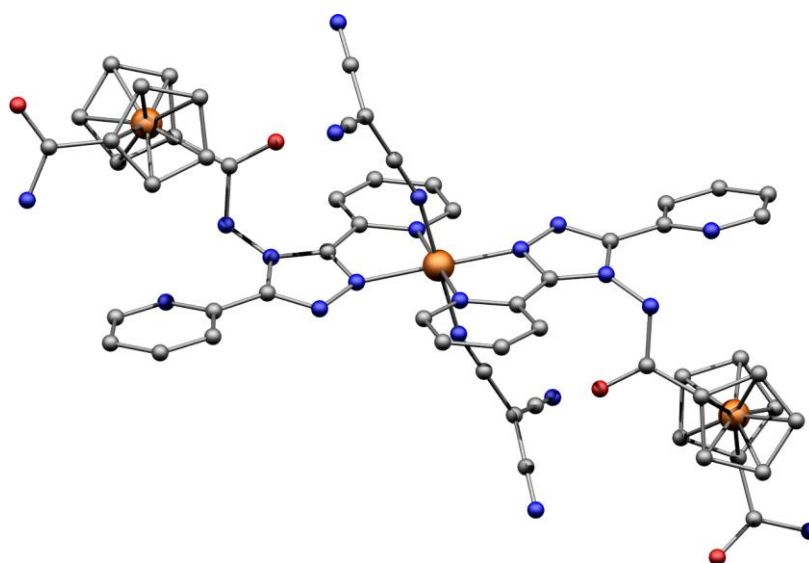


Figure 9. The DFT optimized molecular structure of **1'** in the low-spin state used for the calculation of ^{57}Fe Mössbauer parameters. The atoms are colored as following: iron (orange), nitrogen (blue), oxygen (red), and carbon (dark gray). Hydrogen atoms were omitted for clarity.

Afterwards, TPSSh functional and ORCA 4.2.1 were used to calculate the quadrupole splitting ($\Delta E_Q^{\text{TPSSh}}$) and the electron density at the iron nucleus (ρ_0^{TPSSh})—Table S8. The methodology reported in [37] was then utilized to calculate final values of the isomer shift (δ) and the quadrupole splitting (ΔE_Q) for all studied complexes. Herein, we employed the reported calibration equations for TPSSh functional:

$$\delta = 6225.57816 - 0.52665 \cdot \rho_0^{\text{TPSSh}} \quad (2)$$

$$\Delta E_Q = -0.12779 + 1.03297 \cdot \Delta E_Q^{\text{TPSSh}} \quad (3)$$

The results are summarized in Table 2. Here, the iron ions undergoing the change of the spin state are labelled as {Fe(abpt)}, and the iron ions coordinated to cyclopentadienyl moieties are labelled as {Fe(Cp)}. The isomers shift values are in very good agreement with those measured at 5 K (Table 2) as can be seen for DFT-calculated values $0.54 \text{ mm}\cdot\text{s}^{-1}$ and $1.14 \text{ mm}\cdot\text{s}^{-1}$ for LS and HS {Fe(abpt)} compared to the experimental data $0.41 \text{ mm}\cdot\text{s}^{-1}$ and $1.18 \text{ mm}\cdot\text{s}^{-1}$. Furthermore, the quadrupole splitting parameters are also consistent: $0.63 \text{ mm}\cdot\text{s}^{-1}$ and $3.28 \text{ mm}\cdot\text{s}^{-1}$ for LS and HS {Fe(abpt)} agrees well with the experimental data $0.48 \text{ mm}\cdot\text{s}^{-1}$ and $3.15 \text{ mm}\cdot\text{s}^{-1}$. Also, the values of δ and ΔE_Q for the {Fe(Cp)} fragments are consistent with the experimental data. Therefore, it seems that the DFT-optimized molecular structures of **1'** is appropriate. The same procedure was applied also to the above mentioned $[\text{Fe}(\text{DAPP})(\text{abpt})]^{2+}$ complex (Tables S5 and S6) (DAPP = [bis(3-aminopropyl)(2-pyridylmethyl)amine]), and in this case there is good agreement found for the isomer shifts, whereas larger discrepancies are observed for the quadrupole splitting, which can be most likely assigned to higher temperatures at which the experimental data were acquired—Table 2. Nevertheless, the calculated data are similar to **1'**.

3. Materials and Methods

3.1. Materials and Syntheses

Some of the manipulations were performed under a dry nitrogen or argon atmosphere. All chemicals and solvents were purchased from commercial sources (Across Organics, Sigma-Aldrich, and Lachema) and used as received. Chloroform (CHCl_3) and dichloromethane (DCM) were dried using standard protocols and stored over molecular sieves under an argon atmosphere [38]. The ligand bis(*N*-4-[3,5-di-(2-pyridyl)]-1,2,4-

triazoyl])ferrocene carboxamide (**L**) was synthesized according to modified literature procedures [39,40].

3.1.1. Synthesis of the Ligand (**L**)

In a round three-neck flask 1,1'-ferrocenedicarboxylic acid (548.7 mg, 2.00 mmol) and pyridine (161 μ L, 1.99 mmol) were dissolved in dry CHCl_3 (10 mL) under a nitrogen atmosphere at room temperature. To the well stirred mixture, oxalyl chloride (560 μ L, 6.62 mmol, 3.3 eq) was added dropwise. The reaction mixture was heated to 60 $^\circ\text{C}$ under a reflux condenser for 2 h, and then all volatile solvents were evaporated under vacuum to give a dark red solid of 1,1'-ferrocenyl dichloride. In the next step, 1,1'-ferrocenyl dichloride was used without further purification. It was dissolved in dry DCM (10 mL) under a nitrogen atmosphere, and a solution of 4-amino-3,5-di(pyridyl)-4*H*-1,2,4-triazole (973.6 mg; 4.09 mmol, 2 eq) and pyridine (330 μ L, 4.08 mmol) in dry DCM (10 mL) was added. The reaction mixture was stirred over a period of 48 h at room temperature. The obtained dark orange suspension was washed with 0.01 M HCl (4×10 mL). The organic phase was dried over anhydrous sodium sulfate, filtered, and evaporated in vacuum. The crude product was purified with column chromatography using silica gel and a mixture of CHCl_3 , MeOH and ammonia ($w = 25\%$) in a volume ratio of 15:4:0.5 as a mobile phase. Fractions containing the product ($R_f = 0.75$) were collected. The volatiles were evaporated under reduced pressure. The product was obtained as an orange solid and dried in vacuo overnight. Yield 52% based on 1,1'-ferrocenedicarboxylic acid.

Anal. Calcd. (%) for $\text{C}_{37}\text{H}_{27}\text{Cl}_3\text{Fe}_1\text{N}_{12}\text{O}_2$ ($M_r = 833.89$): C, 53.29; H, 3.26; N, 20.16. Found: C, 53.06; H, 3.64; N, 20.49. ^1H NMR (CDCl_3 , δ) 4.54 (s, 4H, H2), 5.03 (s, 4H, H1), 7.20 (t, 4H, H9, $^3J_{\text{HH}} = 5.87$ Hz), 7.82 (t, 4H, H8, $^3J_{\text{HH}} = 7.43$ Hz), 8.35 (d, 4H, H7, $^2J_{\text{HH}} = 7.83$ Hz), 8.42 (d, 4H, H10, $^2J_{\text{HH}} = 3.91$ Hz), 11.66 (s, 2 H, NH). ^{13}C NMR (CDCl_3 , δ) 70.39 (CH Cp, C1), 72.36 (CH Cp, C2), 73.12 (C Cp, C3), 124.37 (CH pyridyl, C7), 124.80 (CH pyridyl, C9), 137.24 (CH pyridyl, C8), 146.43 (CH pyridyl, C6), 148.21 (CH pyridyl, C10), 151.82 (C triazole, C5), 170.46 (CO, C4). MS (+) m/z : 715.15 [$\text{L1}+\text{H}$] $^+$ ($I_{\text{rel}} = 4\%$); 737.18 [$\text{L1}+\text{Na}$] $^+$ ($I_{\text{rel}} = 100\%$). FT-IR (ATR, cm^{-1}): 3241 br, 1676 vs, 1586 m, 1511 s, 1448 s, 1431 sh, 1375 m, 1310 m, 1278 s, 1138 m, 992 m 791 s, 740 m, 705 m, 693 sh, 604 m, 499 m.

3.1.2. Synthesis of the Complex $\{\text{Fe}(\text{L})(\text{C}(\text{CN})_3)_2\}_n$ (**1**)

Iron(II) chloride tetrahydrate (38.4 mg, 0.19 mmol) was dissolved in 10 mL of a methanol–water mixture (1:1 volume ratio) under an argon atmosphere at room temperature, and then a solution of **L** (158.4 mg; 0.19 mmol) in 50 mL of methanol-DCM (10:1) was added in small portions. The obtained orange solution was stirred for 1 h at room temperature. Then solid potassium tricyanomethanide (50.3 mg; 0.39 mmol) was added, and the reaction mixture was stirred overnight. The product was isolated with centrifugation and washed three times with water. The resulting red powder was dried in a desiccator over NaOH overnight. Yield was 83% based on the ligand **L**.

Anal. Calcd. (%) for $\text{C}_{44}\text{H}_{26}\text{Fe}_2\text{N}_{18}\text{O}_2$ ($M_r = 950.49$): C, 42.16; H, 4.11; N, 6.64. Found: C, 42.08; H, 3.96; N, 6.76. FT-IR (ATR, cm^{-1}): 3407 sh, 3104 br, 2159 vs, 1689 s, 1622 m, 1588 m, 1553 m, 1448 vs, 1432 sh, 1374 m, 1273 s, 994 w, 790 s, 742 m, 698 m, 643 m, 615 m, 562 m, 496 m.

3.2. Analytical Methods

Elemental analysis (C, H, N) was performed on a Flash 2000 CHNO-S Analyzer (Thermo Scientific, Waltham, MA, USA). Infrared spectra (IR) were recorded on a Jasco FT/IR-4700 spectrometer (Jasco, Easton, MD, USA) using the ATR technique on a diamond plate in the range 400–4000 cm^{-1} . Electronic spectra were recorded on a Cintra 3030 (GBC Scientific Instruments, IL, USA) spectrometer with 10 mm path length quartz cuvettes in dichloromethane. The mass spectra (MS) were collected on a LCQ Fleet Ion Mass Trap mass spectrometer (Thermo Scientific, Waltham, MA, USA) equipped with an electrospray ion source and a three-dimensional ion-trap detector in the positive mode. Cyclic voltammetry

(CV) measurements were carried out using an electrochemical analyzer CHI600C (CH Instrument, Austin, TX, USA) with a three-electrode-type cell. A glassy carbon working electrode, a platinum wire auxiliary electrode, and a Ag/Ag⁺ reference electrode (0.01 M AgNO₃ in 0.1 M TBAP, CH₃CN) were used during the measurements. The internal Fc/Fc⁺ standard ($E_{1/2} = 0.077$ V vs. reference electrode, $E_{1/2} = 0.624$ V vs. SHE) was employed in order to obtain the final potential values referred to SHE [41]. The measurements were performed under an inert argon atmosphere in an acetonitrile solution containing tetrabutylammonium perchlorate (TBAP), as a supporting electrolyte. The ¹H and ¹³C NMR spectra were recorded at 298 K on a Varian 400 MHz NMR spectrometer (Varian, Palo Alto, CA, USA) operating at 399.95 MHz (¹H) and 100.60 MHz (¹³C). The signal assignments in ¹H and ¹³C NMR spectra were based in part on two-dimensional COSY, HMBC and HMQC experiments. The multiplicity of the signals was indicated as follows: s—singlet, d—doublet, and t—triplet. The transmission ⁵⁷Fe Mössbauer spectrum of complex **1** was measured with laboratory Mössbauer spectrometer with a ⁵⁷Co(Rh) radiation source. The Mössbauer spectrum was fitted with the Lorentzian line shapes using MossWinn 4.0 program. The isomer shift values were referred to the 28 μm α-Fe foil (Ritverc). For the low-temperature Mössbauer measurement (5–300 K), the sample was placed inside the closed-cycle cryogen-free cryogenic system for Mössbauer spectroscopy (Cryostation, Montana Instruments). The magnetometry was performed using a low temperature vibrating sample magnetometer (Cryogenic Limited) in the temperature range 2–300 K in the magnetic field of 0.2 T. The experimental data were corrected for the diamagnetism of the sample and for the diamagnetism of the sample holder.

3.3. X-ray Crystallography

Single crystals of **L** for X-ray structure analysis were prepared with slow evaporation of a chloroform-methanol solution. Data collection for **L** was done using an XtaLAB Synergy-I diffractometer with a HyPix3000 hybrid pixel array detector and microfocused PhotonJet-I X-ray source (Cu Kα). The structure was solved using SHELXT [42] program and refined through the full matrix least-squares procedure with Olex2.refine [43] in OLEX2 (version 1.5) [44]. The multi-scan absorption corrections were applied using the program CrysAlisPro 1.171.40.82a [45]. Figures with detailed structure features were drawn using Diamond software [46]. Non-routine aspects of crystal structure determination and refinement are as follows: The isolated single-crystals were of a poor quality, and this affected the data collection. We collected complete a data set for diffractions only up to resolution 0.88 Å. One of the abpt moieties **L** exhibited positional disorder that was modeled as disorder over two positions (ratio of occupational factors: 0.55:0.45).

The crystallographic data and refinement data for **L** are as follows: C₃₆H₂₈FeN₁₂O₃, $M_r = 732.55$, $T = 298(2)$ K, light orange color, $0.23 \times 0.13 \times 0.10$ mm³, monoclinic, space group $P2_1/c$, $a = 7.8354(3)$, $b = 19.2990(7)$, $c = 22.5050(12)$ Å, $\alpha = 90^\circ$, $\beta = 90.709(5)^\circ$, $\gamma = 90^\circ$, $V = 3402.8(3)$ Å³, $Z = 4$, $D_{\text{calc}} = 1.430$ g·cm⁻³, $F_{000} = 1512$, 15,556 reflections collected, 5992 unique ($R_{\text{int}} = 0.0435$), $\text{GoF} = 1.169$, $R_1 = 0.0892$, $wR_2 = 0.1722$, R indices calculated with $I > 2s(I)$. CSD deposition number: 2177052. Selected bond lengths and angles are shown in Table 1.

3.4. Theoretical Calculations

The ORCA 4.2 or ORCA 5.0 software was used for all quantum chemical calculations [47,48]. The molecular geometries were optimized with ORCA 5.0 using the polarized triple- ζ quality basis set def2-TZVP for all atoms, except carbon and hydrogen atoms for which the def2-SVP basis set was applied [49]. The calculations utilized the Split-RI-J Coulomb approximation [50] with the auxiliary basis sets def2/J [51]. Increased integration grids (DEFGRID3) and tight SCF convergence criteria were used in all calculations. The meta-GGA functional TPSS was employed together with the atom-pairwise dispersion correction (D3BJ) [52,53]. The geometry optimization was not done in vacuum but using a SMD solvation model [54]. Moreover, the tight optimization criteria were required

(TightOpt), and all convergence criteria must have been fulfilled (EnforceStrictConvergence was set to True). The vibrational analyses confirmed proper convergence for complexes at local energy minimum (no imaginary frequencies)—Table S7. The subsequent calculations utilized hybrid meta-GGA functional TPSSh [55,56] together with the chain-of-spheres (RIJCOSX) approximation to exact exchange [57,58] as implemented in ORCA.

4. Conclusions

In conclusion, we have designed, synthesized, and characterized with different spectral analyses a new ferrocene-based metalloligand with two triazole carboxamide pendant arms **L** and presumable polymeric Fe^{II} complex **1**. The structure of **L** was characterized through single crystal X-ray structure analysis. Magnetic data and ⁵⁷Fe Mössbauer spectra of **1** confirmed the presence of the mixture of low- and high-spin species. For better understanding of the electronic spectra of **L**, as well as magnetic properties and Mössbauer spectra of complex **1**, theoretical calculations were performed.

Supplementary Materials: The following supporting information can be downloaded at: <https://www.mdpi.com/article/10.3390/inorganics10110199/s1>, Figure S1: ¹H-¹H g-COSY NMR spectrum of **L**; Figure S2: ¹H-¹³C g-HMQC NMR spectrum of **L**; Figure S3: ¹H-¹³C g-HMBC NMR spectrum of **L**; Figure S4: Comparison of FTIR spectra of studied ligand (**L**) and complex (**1**); Figure S5: (a) Representation of the two-dimensional hydrogen-bonding network in the crystal structure of **L**. The network of interconnected neighboring molecules of **L** is parallel with the plane *ac*. (b) Representation of the final three-dimensional network created through interconnection of layers with C–H⋯π interactions. The layers are colored for clarity (orange and green); Figure S6: The UV-Vis absorption spectrum of ligand **L** in DCM solution with molar concentrations *c* = 2.1 mmol/dm³ (top) and *c* = 43.2 μmol/dm³ (bottom); Table S1: Crystal data and structure refinements for **L**; Table S2: The XYZ coordinates of the molecular structure of **L** optimized with DFT; Table S3: The XYZ coordinates of the molecular structure of **1'** in the low-spin state optimized with DFT; Table S4: The XYZ coordinates of the molecular structure of **1'** in the high-spin state optimized with DFT; Table S5: The XYZ coordinates of the molecular structure of [Fe(DAPP)(abpt)]²⁺ in the low-spin state optimized with DFT; Table S6: The XYZ coordinates of the molecular structure of [Fe(DAPP)(abpt)]²⁺ in the high-spin state optimized with DFT; Table S7: The list of calculated frequencies for DFT optimized molecular structures in Tables S2–S7; Table S8: The list of TPSSh calculated values of the electron density at the iron nucleus and the quadrupole splitting for DFT optimized molecular structures in Tables S3–S7.

Author Contributions: Conceptualization, P.A., I.N., J.P. and R.H.; methodology, P.A., I.N., J.P. and R.H.; writing—original draft preparation, P.A. and R.H.; writing—review and editing, P.A., I.N., J.P. and R.H. All authors have read and agreed to the published version of the manuscript.

Funding: The authors (P.A., R.H., I.N.) acknowledge the financial support from institutional sources of the Department of Inorganic Chemistry and Palacký University Olomouc, Czech Republic and from the Czech Science Foundation (Grant No. 17-08992S). J.P. acknowledge the financial support from institutional sources of the Department of Experimental Physics and Palacký University Olomouc, Czech Republic. We also acknowledge CzechNanoLab Research Infrastructure supported by MEYS CR (LM2018110) for the measurement of the magnetic data for **1**.

Data Availability Statement: Supplementary crystallographic data for compound **L** is given in CCDC number 2177052. These data can be obtained free of charge from The Cambridge Crystallographic Data Centre via www.ccdc.cam.ac.uk/data_request/cif (accessed on 21 September 2022).

Acknowledgments: The authors acknowledge Lubomír Havlíček for the measurement of the magnetic data for **1**, Lukáš Kouřil for his help with the Mössbauer spectra, and Radka Křikavová for language corrections.

Conflicts of Interest: The authors declare that they have no known competing financial interest or personal relationship that could have appeared to influence the work reported in this paper.

References

1. Kumar, G.; Gupta, R. Molecular designed architectures—the metalloligand way. *Chem. Soc. Rev.* **2013**, *42*, 9403–9453. [[CrossRef](#)] [[PubMed](#)]
2. Kumar, G.; Kumar, G.; Gupta, R. Effect of pyridyl donors from organic ligands: Versus metalloligands on material design. *Inorg. Chem. Front.* **2021**, *8*, 1334–1373. [[CrossRef](#)]
3. Gao, W.-X.; Zhang, H.-N.; Jin, G.-X. Supramolecular catalysis based on discrete heterometallic coordination-driven metallacycles and metallacages. *Coord. Chem. Rev.* **2019**, *386*, 69–84. [[CrossRef](#)]
4. Cook, T.R.; Stang, P.J. Recent Development in the Preparation and Chemistry of Metallacycles and Metallacages via Coordination. *Chem. Rev.* **2015**, *115*, 7001–7045. [[CrossRef](#)] [[PubMed](#)]
5. Horikoshi, R.; Mochida, T. Ferrocene-containing coordination polymers: Ligand design and assembled structure. *Eur. J. Inorg. Chem.* **2010**, *2010*, 5355–5371. [[CrossRef](#)]
6. Jensen, T.; Pedersen, H.; Bang-Andersen, B.; Madsen, R.; Jørgensen, M. Palladium-catalysed aryl amination-heck cyclization cascade: A one-flask approach to 3-substituted indoles. *Angew. Chem. Int. Ed.* **2008**, *47*, 888–890. [[CrossRef](#)]
7. Štěpnička, P. Phoshino-carboxamides: The inconspicuous gems. *Chem. Soc. Rev.* **2012**, *41*, 4273–4305. [[CrossRef](#)]
8. Xie, Y.; Lin, R.-B.; Chen, B. Old Materials for New Functions: Recent Progress on Metal Cyanide Based Porous Materials. *Adv. Sci.* **2022**, *9*, 92104234. [[CrossRef](#)]
9. Seredyuk, M.; Gaspar, A.B.; Ksenofontov, V.; Reiman, S.; Galyametdinov, Y.; Haase, W.; Rentschler, E.; Gülich, P. Multifunctional materials exhibiting spin crossover and liquid-crystalline properties. *Hyperfine Interact.* **2005**, *166*, 385–390. [[CrossRef](#)]
10. Javed, M.K.; Sulaiman, A.; Yamashita, M.; Li, Z.-Y. Shedding light on bifunctional luminescent spin crossover materials. *Coord. Chem. Rev.* **2022**, *467*, 214625. [[CrossRef](#)]
11. Lacroix, P.G.; Malfant, I.; Real, J.-A.; Rodriguez, V. From magnetic to nonlinear optical switches in spin-crossover complexes. *Eur. J. Inorg. Chem.* **2013**, *2013*, 615–627. [[CrossRef](#)]
12. Scott, H.S.; Gartshone, C.J.; Guo, S.-X.; Moubaraki, B.; Bond, A.M.; Batten, S.R.; Murray, K.S. Ferrocen-appended ligands for use in spin crossover-redox “hybrid” complexes of iron(ii) and cobalt (ii). *Dalton Trans.* **2014**, *43*, 15212–15220. [[CrossRef](#)] [[PubMed](#)]
13. Moliner, N.; Gaspar, A.B.; Muñoz, M.C.; Niel, V.; Cano, J.; Real, J.A. Light- and thermal-induced spin crossover in {Fe(abpt)₂[N(CN)₂]₂}. Synthesis, structure, magnetic properties, and high-spin–low-spin relaxation studies. *Inorg. Chem.* **2001**, *40*, 3986–3991. [[CrossRef](#)] [[PubMed](#)]
14. Dupouy, G.; Marchivie, M.; Triki, S.; Sala-Pala, J.; Gómez-Garcia, C.J.; Pillet, S.; Lecomte, C.; Létard, J.-F. Photoinduced HS state in the first spin-crossover chain containing a cyanocarbanion as bridging ligand. *Chem. Commun.* **2009**, *23*, 3404–3406. [[CrossRef](#)]
15. Gasser, G.; Carr, J.D.; Coles, S.J.; Green, S.J.; Hursthouse, M.B.; Cafferkey, S.M.; Stoeckli-Evans, H.; Tucker, J.H.R. Synthesis and complexation properties of novel triazolyl-based ferrocenyl ligands. *J. Organomet. Chem.* **2010**, *695*, 249–255. [[CrossRef](#)]
16. Braga, D.; Polito, M.; Giaffreda, S.L.; Grepioni, F. Novel organometallic building blocks for molecular crystal engineering. Part 4, Synthesis and characterization of mono- And bis-amido derivatives of [Co^{III}(η⁵-C₅H₄COOH)₂]⁺ and their utilization as ligands. *Dalton Trans.* **2005**, *34*, 2766–2773. [[CrossRef](#)]
17. Meng, X.; Li, G.; Hou, H.; Han, H.; Fan, Y.; Zhu, Y.; Du, C. A series of metal-ferrocenedicarboxylate coordination polymers: Crystal structures, magnetic and luminescence properties. *J. Organomet. Chem.* **2003**, *679*, 153–161. [[CrossRef](#)]
18. Kühnert, J.; Rüffer, T.; Ecorchard, P.; Bräuer, B.; Lan, Y.; Powell, A.K.; Lang, H. Reaction chemistry of 1,1'-ferrocenedicarboxylate towards M(ii) salts (M = Co, Ni, Cu): Solid-state structure and electrochemical, electronic and magnetic properties of bis- and tetrametallic complexes and coordination polymers. *Dalton Trans.* **2009**, *38*, 4499–4508. [[CrossRef](#)]
19. Khirid, S.; Jangid, D.K.; Biswas, R.; Meena, S.; Sahoo, S.C.; Verma, V.P.; Nandi, C.; Halder, K.K.; Dhayal, R.S. Ferrocene decorated homoleptic silver(I) clusters: Synthesis, structure, and their electrochemical behaviour. *J. Organomet. Chem.* **2021**, *948*, 121923. [[CrossRef](#)]
20. Wei, K.-J.; Ni, J.; Liu, Y. Heterobimetallic Metal-Complex Assemblies Constructed from the Flexible Arm-Like Ligand 1,1'-Bis[(3-pyridylamino)carbonyl]ferrocene: Structural Versatility in the Solid State. *Inorg. Chem.* **2010**, *49*, 1834–1848. [[CrossRef](#)]
21. Cao, C.-Y.; Wei, K.-J.; Ni, J.; Liu, Y. Solvent-induced two heterometallic coordination polymers based on a flexible ferrocenyl ligand. *Inorg. Chem. Commun.* **2010**, *13*, 19–21. [[CrossRef](#)]
22. Djaković, S.; Maračić, S.; Lapić, J.; Kovalski, E.; Hildebrandt, A.; Lang, H.; Vrček, V.; Raić-Malić, S.; Cetina, M. Triazole-tethered ferrocene-quinoline conjugates: Solid-state structure analysis, electrochemistry and theoretical calculations. *Struc. Chem.* **2021**, *32*, 2291–2301. [[CrossRef](#)]
23. Navrátil, M.; Císařová, I.; Štěpnička, P. Synthesis, Coordination and Electrochemistry of a Ferrocenyl-Tagged Aminobisphosphane Ligand. *Eur. J. Inorg. Chem.* **2021**, *2021*, 3781–3792. [[CrossRef](#)]
24. Okabe, T.; Nakazaki, K.; Igaue, T.; Nakamura, N.; Donnio, D.; Guillon, D.; Gallani, J.-L. Synthesis and physical properties of ferrocene derivatives. XXI Crystal structure of a liquid crystalline ferrocene derivative, 1,1'-bis [3-[4-(4-methoxyphenoxy)carbonyl]phenoxy]propyloxycarbonyl]ferrocene. *J. Appl. Cryst.* **2009**, *42*, 63–68. [[CrossRef](#)]
25. Kowalski, K.; Szczupak, Ł.; Skiba, J.; Abbel-Rahman, O.S.; Winter, R.F.; Czerwieńiec, R.; Therrien, B. Synthesis, structure, and spectroelectrochemistry of ferrocenyl-meldrum’s acid donor-acceptor systems. *Organometallics* **2014**, *33*, 4697–4705. [[CrossRef](#)]
26. Labulo, A.H.; Omondi, B.; Nyamori, V. Synthesis, crystal structures and electrochemical properties of ferrocenyl imidazole derivatives. *Heliyon* **2019**, *5*, e02580. [[CrossRef](#)]

27. Zhang, E.; Hou, H.; Meng, X.; Liu, Y.; Liu, Y.; Fan, Y. Ferrocenyl functional coordination polymers based on mono-, bi-, and heterotrinnuclear organometallic building blocks: Syntheses, structures, and properties. *Cryst. Growth. Des.* **2009**, *9*, 903–913. [[CrossRef](#)]
28. Reynes, O.; Maillard, F.; Moutet, J.-C.; Royal, G.; Saint-Aman, E.; Stanciu, G.; Dutasta, J.-P.; Gosse, I.; Mulatier, J.-C. Complexation and electrochemical sensing of anions by amide-substituted ferrocenyl ligands. *J. Organomet. Chem.* **2001**, *637–639*, 356–363. [[CrossRef](#)]
29. Magalhães, C.I.R.; Gomes, A.C.; Lopes, A.D.; Gonçalves, I.S.; Pillinger, M.; Jin, E.; Kim, I.; Ko, Y.H.; Kim, K.; Nowik, I.; et al. Ferrocene and ferrocenium inclusion compounds with cucurbiturils: A study of metal atom dynamics probed by Mössbauer spectroscopy. *Phys. Chem. Chem. Phys.* **2017**, *19*, 21548–21555. [[CrossRef](#)]
30. Siebler, D.; Linseis, M.; Gasi, T.; Carrella, L.M.; Winter, R.F.; Förster, C.; Heinze, K. Oligonuclear ferrocene amides: Mixed-valent peptides and potential redox-switchable foldamers. *Chem. Eur. J.* **2011**, *17*, 4540–4551. [[CrossRef](#)]
31. Gütllich, P.; Enslin, J. *Inorganic Electronic Structure and Spectroscopy*; Solomon, E.I., Lever, A.B.P., Eds.; Wiley: New York, NY, USA, 1999; Volume I, p. 161.
32. Greenwood, N.N.; Gibb, T.C. *Mössbauer Spectroscopy*; Chapman and Hall Ltd.: London, UK, 1971.
33. Matouzenko, G.S.; Bousseksou, A.; Borshch, S.A.; Perrin, M.; Zein, S.; Salmon, L.; Molnar, G.; Lecocq, S. Cooperative Spin Crossover and Order-Disorder Phenomena in a Mononuclear Compound [Fe(DAPP)(abpt)](ClO₄)₂[DAPP = [Bis(3-aminopropyl)(2-pyridylmethyl)amine], abpt = 4-Amino-3,5-bis(pyridin-2-yl)-1,2,4-triazole]. *Inorg. Chem.* **2004**, *43*, 227–236. [[CrossRef](#)] [[PubMed](#)]
34. Herchel, R.; Trávníček, Z.; Zbořil, R. Tuning of the critical temperature in iron(II) spin-crossover materials based on bridging polycyanidometallates: Pentacyanidonitrosylferrate(II) and hexacyanidoplatinate(IV). *Inorg. Chem.* **2011**, *50*, 12390–12392. [[CrossRef](#)] [[PubMed](#)]
35. Lu, T.; Chen, F. Multiwfn: A multifunctional wavefunction analyzer. *J. Comput. Chem.* **2012**, *33*, 580–592. [[CrossRef](#)] [[PubMed](#)]
36. Liu, Z.; Wang, X.; Lu, T.; Yuan, A.; Yan, X. Potential optical molecular switch: Lithium@cyclo[18]carbon complex transforming between two stable configurations. *Carbon* **2022**, *187*, 78–85. [[CrossRef](#)]
37. Gallenkamp, C.; Kramm, U.I.; Proppe, J.; Krewald, V. Calibration of computation Mössbauer spectroscopy to unravel active sites in FeNC catalysts for the oxygen reduction reaction. *Int. J. Quantum Chem.* **2021**, *121*, e26394. [[CrossRef](#)]
38. Armarego, W.L.F.; Chai, C. *Purification of Laboratory Chemicals*, 6th ed.; Butterworth-Heinemann, Elsevier: Oxford, UK, 2009.
39. Miyaji, H.; Dudic, M.; Gasser, G.; Green, S.J.; Moran, N.; Prokeš, I.; Labat, G.; Stoeckli-Evans, H.; Strawbridge, S.M.; Tucker, J.H.R. A heterodifunctionalised ferrocene derivatives that self-assembles in solution through complementary hydrogen-bonding interactions. *Dalton Trans.* **2004**, *33*, 2831–2832. [[CrossRef](#)]
40. Petrov, A.R.; Jess, K.; Freytag, M.; Jones, P.G.; Tamm, M. Large-scale preparation of 1,1'-ferrocenedicarboxylic acids, a key compound for the synthesis of 1,1'-disubstituted ferrocene derivatives. *Organometallics* **2013**, *32*, 5946–5954. [[CrossRef](#)]
41. Pavlishchuk, V.V.; Addison, A.W. Conversion constants for redox potentials measured versus different reference electrodes in acetonitrile solutions at 25 °C. *Inorg. Chim. Acta* **2000**, *298*, 97–102. [[CrossRef](#)]
42. Sheldrick, G.M. Crystal structure refinement with SHELXL. *Acta Crystallogr. Sect. A* **2015**, *71*, 3–8. [[CrossRef](#)]
43. Bourhis, L.J.; Dolomanov, O.V.; Gildea, R.J.; Howard, J.A.K.; Puschmann, H. The anatomy of a comprehensive constrained, restrained refinement program for the modern computing environment—Olex2, dissected. *Acta Crystallogr. Sect. A* **2015**, *71*, 59–75. [[CrossRef](#)]
44. Dolomanov, O.V.; Bourhis, L.J.; Gildea, R.J.; Howard, J.A.K.; Puschmann, H. OLEX2: A complete structure solution, refinement and analysis. *J. Appl. Crystallogr.* **2009**, *42*, 339–341. [[CrossRef](#)]
45. Rigaku Oxford Diffraction (2020) CrysAlisPro 1.171.40.82a. Available online: <http://www.rigaku.com/> (accessed on 12 September 2020).
46. Brandenburg, K.; Putz, H. *Diamond—Crystal and Molecular Structure Visualization, ver. 2.1.b*; Crystal Impact GbR: Bonn, Germany, 1999.
47. Neese, F. Software update: The ORCA program system, version 4.0. *Wiley Interdiscip. Rev. Comput. Mol. Sci.* **2018**, *8*, e1327. [[CrossRef](#)]
48. Neese, F. Software update: The ORCA program system—Version 5.0. *Wiley Interdiscip. Rev. Comput. Mol. Sci.* **2022**, *12*, e1606. [[CrossRef](#)]
49. Weigend, F.; Ahlrichs, R. Balanced basis sets of split valence, triple zeta valence and quadruple zeta valence quality for H to Rn: Design and assessment of accuracy. *Phys. Chem. Chem. Phys.* **2005**, *7*, 3297–3305. [[CrossRef](#)]
50. Neese, F. An Improvement of the Resolution of the Identity Approximation for the Formation of the CuLomb Matrix. *J. Comp. Chem.* **2003**, *24*, 1740–1747. [[CrossRef](#)] [[PubMed](#)]
51. Weigend, F. Accurate Coulomb-fitting basis sets for H to Rn. *Phys. Chem. Chem. Phys.* **2006**, *8*, 1057–1065. [[CrossRef](#)]
52. Grimme, S.; Ehrlich, S.; Goerigk, L. Effect of the damping function in dispersion corrected density functional theory. *J. Comput. Chem.* **2011**, *32*, 1456–1465. [[CrossRef](#)]
53. Grimme, S.; Antony, J.; Ehrlich, S.; Krieg, H. A consistent and accurate ab initio parametrization of density functional dispersion correction (DFT-D) for the 94, elements H-Pu. *J. Chem. Phys.* **2010**, *132*, 154104. [[CrossRef](#)]

54. Marenich, A.V.; Cramer, C.J.; Truhlar, D.G. Universal solvation model based on solute electron density and on a continuum model of the solvent defined by the bulk dielectric constant and atomic surface tensions. *J. Phys. Chem. B* **2009**, *113*, 6378–6396. [[CrossRef](#)]
55. Perdew, J.P.; Kurth, S.; Zupan, A.; Blaha, P. Accurate density functional with correct formal properties: A step beyond the generalized gradient approximation. *Phys. Rev. Lett.* **1999**, *82*, 2544–2547. [[CrossRef](#)]
56. Perdew, J.P.; Tao, J.; Staroverov, V.N.; Scuseria, G.E. Meta-generalized gradient approximation: Explanation of a realistic nonempirical density functional. *J. Chem. Phys.* **2004**, *120*, 6898–6911. [[PubMed](#)]
57. Neese, F.; Wennmohs, F.; Hansen, A.; Becker, U. Efficient, approximate and parallel Hartree–Fock and hybrid DFT calculations. A ‘chain-of-spheres’ algorithm for the Hartree–Fock exchange. *Chem. Phys.* **2009**, *356*, 98–109. [[CrossRef](#)]
58. Izsák, R.; Neese, F. An overlap fitted chain of spheres exchange method. *J. Chem. Phys.* **2011**, *135*, 144105. [[CrossRef](#)] [[PubMed](#)]